

Article

Gaining a New Technological Readiness Level for Laser-Structured Electrodes in High-Capacity Lithium-Ion Pouch Cells

Alexandra Meyer ¹, Penghui Zhu ¹, Anna Smith ² and Wilhelm Pfleging ^{1,*}

¹ Institute for Applied Materials—Applied Materials Physics (IAM-AWP), Karlsruhe Institute of Technology, 76344 Eggenstein-Leopoldshafen, Germany; alexandra.meyer@kit.edu (A.M.); penghui.zhu@kit.edu (P.Z.)

² Institute for Applied Materials—Energy Storage Systems (IAM-ESS), Karlsruhe Institute of Technology, 76344 Eggenstein-Leopoldshafen, Germany; anna.smith@kit.edu

* Correspondence: wilhelm.pfleging@kit.edu

Abstract: For the first time, the laser structuring of large-footprint electrodes with a loading of 4 mAh cm^{-2} has been validated in a relevant environment, including subsequent multi-layer stack cell assembly and electrochemical characterization of the resulting high-capacity lithium-ion pouch cell prototypes, i.e., a technological readiness level of 6 has been achieved for the 3D battery concept. The structuring was performed using a high-power ultrashort-pulsed laser, resulting in well-defined line structures in electrodes without damaging the current collector, and without melting or altering the battery active materials. For cells containing structured electrodes, higher charge and discharge capacities were measured for C-rates $> 1\text{C}$ compared to reference cells based on unstructured electrodes. In addition, cells with structured electrodes showed a three-fold increase in cycle lifetime at a C-rate of 1C compared to those with reference electrodes.

Keywords: lithium-ion batteries; laser manufacturing; upscaling



Citation: Meyer, A.; Zhu, P.; Smith, A.; Pfleging, W. Gaining a New Technological Readiness Level for Laser-Structured Electrodes in High-Capacity Lithium-Ion Pouch Cells. *Batteries* **2023**, *9*, 548. <https://doi.org/10.3390/batteries9110548>

Academic Editor: Pascal Venet

Received: 2 August 2023

Revised: 3 November 2023

Accepted: 7 November 2023

Published: 9 November 2023



Copyright: © 2023 by the authors. Licensee MDPI, Basel, Switzerland. This article is an open access article distributed under the terms and conditions of the Creative Commons Attribution (CC BY) license (<https://creativecommons.org/licenses/by/4.0/>).

1. Introduction

To increase the power density of batteries, a three-dimensional (3D) micro-battery concept was first proposed by Long et al. [1], laying the foundation for subsequent research and development in this area. The 3D battery concept was applied to different electrode types, for example, for lithium-ion cells, leading to improvements in various aspects of battery performance. To apply this concept to electrodes for lithium-ion cells, many researchers are using laser ablation or laser-assisted surface modification. A key advantage of the 3D electrode architecture in lithium-ion cells is its ability to improve the wetting with the liquid electrolyte [2–5], as well as the more homogeneous lithium distribution in the electrodes during cycling [6,7]. The ionic, electronic, and charge transfer resistance are decreased as well as the tortuosity [3,4,6–8]. All these phenomena play a vital role in enhancing the overall performance of the lithium-ion battery, including increasing the specific capacity at elevated C-rates (which denotes the charge or discharge current related to the nominal capacity of the battery in ampere hours) and battery lifetime. These advances have been experimentally proven and validated, as presented in [4,8–14], demonstrating the potential of the 3D battery concept.

Moreover, the application of silicon as an anode active material [4,15–17] and the utilization of thick-film electrodes [3,4,18–20] have been greatly facilitated by the 3D battery design. Various electrode compositions, incorporating different active materials, thicknesses, and patterns, have been manufactured and characterized. However, it is important to note that the realization of small-scale batteries with capacities up to 2.9 Ah [11], so-called lab-pouch cells, has so far been the limit of practical implementation.

In this study, we present a significant breakthrough in the field of high-capacity lithium-ion batteries by employing laser-patterned electrodes. Utilizing a high-power

ultrashort-pulsed (USP) laser source, we have successfully achieved the fabrication of line structures within the electrodes. This innovative approach has enabled the assembly and characterization of high-capacity lithium-ion batteries with a nominal capacity of 16.1 Ah. It is noteworthy that this work not only pushes the boundaries of the current state of the art but also elevates the laser-assisted 3D battery concept to a technology readiness level of 6, signifying its significant progress toward real-world high-energy applications.

By achieving this milestone, our research provides a critical foundation for further investigation, development, and process upscaling in the field of 3D battery technology. The successful realization of high-capacity lithium-ion batteries with laser-patterned electrodes marks a pivotal moment, paving the way for the eventual integration of this promising technology into the industrial production of next-generation batteries. The implications of this advancement are profound, as it holds the potential to revolutionize energy storage systems, leading to improved performance, increased power densities, and extended battery lifetimes.

The findings from this study are expected to significantly contribute to the ongoing efforts in advancing battery technology and accelerating the transition toward a more sustainable and efficient energy landscape.

2. Materials and Methods

Commercially available $\text{LiNi}_{0.6}\text{Mn}_{0.2}\text{Co}_{0.2}\text{O}_2$ (NMC 622) cathodes and graphite anodes were laser patterned and subsequently assembled in high-capacity pouch cells. The cathodes had a thickness of approximately 85 μm per side with a mass loading of 250 g m^{-2} (areal capacity of 4.1 mAh cm^{-2} measured at C/10 using half cells containing NMC 622 vs. Li), being coated on a 15 μm aluminum current collector. The corresponding anodes had a film thickness of 85 μm with a mass loading of 125 g m^{-2} (areal capacity of 4.4 mAh cm^{-2} measured at C/10) and were coated on an 18 μm copper foil. The n/p ratio, the nominal capacity ratio of the negative to the positive electrode, of the unstructured electrodes was 1.1.

The electrodes were laser patterned from roll-to-roll (R2R) using an ultrashort-pulsed laser (FX600, EdgeWave GmbH, Würselen, Germany) with a pulse length of 600 fs, a wavelength of 1030 nm, and a maximal power of 330 W in a multi-process laser patterning workstation (MSV203, M-Solv Ltd., Eynsham, United Kingdom). The laser powers used for the patterning were 94 W and 37 W, with scanning velocities of 5 m s^{-1} and 20 m s^{-1} , 14 and 45 scans, and pitches of 200 μm and 400 μm for the cathodes and anodes, respectively. The laser had a beam diameter of 27.2 μm in the work plane and a repetition rate of 1 MHz was applied. The applied laser pulse peak fluences were therefore calculated to be 26.6 J cm^{-2} and 10.5 J cm^{-2} for the cathodes and anodes, respectively. The process of electrode laser patterning was undertaken through employment of the multi-process R2R laser patterning instrument MSV203 using a step-and-repeat method. A beam expansion telescope of 6-fold magnification was applied to widen the raw beam of 2.6 mm diameter. A scanner (intelliSCAN III 20, Scanlab, Puchheim, Germany) was integrated with an f-theta lens (JENar Silverline, Jenoptik Optical Systems, Jena, Germany), which had a focal length of 255 mm. An exhaust frame was placed directly above the ablation area in order to avoid any material redeposition on the electrode surface. The electrodes were characterized regarding the ablation depth, structure width, debris formation, and potential crack generation using a scanning electron microscope (Phenom XL, Thermo Fisher Scientific, Waltham, MA, USA) and a digital microscope (VHX7000, Keyence, Osaka, Japan). Energy-dispersive X-ray spectroscopy (EDX) mapping was conducted on the cathodes' surface to confirm the composition.

Three prototype pouch cells with a nominal capacity of 20.2 Ah (unstructured electrodes) and two pouch cells with a nominal capacity of 16.1 Ah (structured electrodes) were assembled following the protocol described in [21], each containing nine double-sided coated cathodes (footprint of 135 mm \times 200 mm) and ten double-sided coated anodes (footprint of 139 mm \times 212 mm). To guarantee that all cathode areas were covered by the

anode, an overhang of at least 2 mm was realized by choosing the mentioned electrode dimensions. Ceramic-coated polyester separators (FS 3011-23, Freudenberg GmbH, Weinheim, Germany) with a thickness of 23 μm were used. The stacks with a height of 4 mm were dried at 130 °C for 24 h, and the tabs were welded on the current collector and sealed in an aluminum laminate pouch bag. An amount of 70 mL of electrolyte (LP57 + 5 wt.% FEC) was added.

The current at n-C was calculated considering 1C currents of 20.2 A and 16.1 A for cells with unstructured and laser-structured electrodes, respectively. After 24 h wetting at 40 °C, electrochemical priming was performed by applying three full cycles at C/20 (constant current (CC)–constant voltage (CV) procedure for charge with C/50 as cut-off current; CC C/20 for discharge, symmetrical). Symmetric rate capability measurements (CCCV) were conducted with C-rates of C/10 and C/5 (five cycles each), where the cut-off current corresponded to a C-rate of C/20. Ten cycles each followed at the C-rates C/2, 1C, 2C, 3C, and 5C with a cut-off current corresponding to a C-rate of C/10. Finally, five cycles of C/5 were conducted as a measure of degradation effects caused by the rate capability analysis. Lifetime measurements with a C-rate of 1C (CCCV with cut-off current C/10 for charge, CC for discharge, symmetrical) followed. The voltage window for all measurements was 3.0 V to 4.2 V, and they were performed using a battery cycler (MRS-system, Basytec GmbH, Asselfingen, Germany). To perform the measurements under safe conditions, a sealed aluminum test box was applied. The temperature inside the box was controlled with the help of a cryostat connected to a stainless-steel plate.

3. Results and Discussion

Commercial electrodes were subjected to laser patterning and the scanning electron microscopy (SEM) images are shown in Figure 1a–f. The cathode primary particles have a size of $0.98 \pm 0.32 \mu\text{m}$ (median 0.96 μm) and the secondary particles have a mean size of $3.89 \pm 0.95 \mu\text{m}$ (median 3.83 μm). The graphite particles in the anode have a mean size of $17.94 \pm 5.9 \mu\text{m}$ (median 16.93 μm) and a chamfered appearance. No cracks or debris is observed close to the laser-generated channel structures. For the anodes, some particles remain within the channels. The depths of the channels are $53.9 \pm 9.4 \mu\text{m}$ and $88.4 \pm 2.2 \mu\text{m}$, the widths are $34.9 \pm 2.7 \mu\text{m}$ and $58.7 \pm 1.8 \mu\text{m}$, the aspect ratios are 1.54 and 1.50, and the mass loss of the coating is 8.9% and 22.3% for the anode and cathode, respectively. The n/p ratio after laser patterning is 1.24.

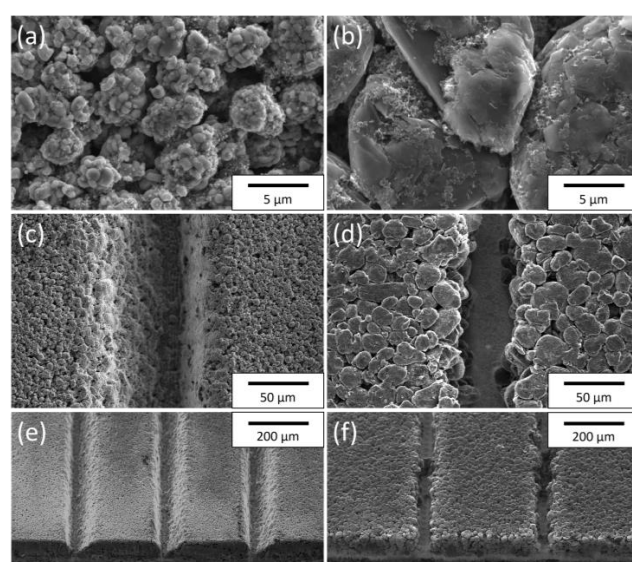


Figure 1. SEM images of the laser-patterned electrodes: (a) cathode surface, (b) anode surface, (c) line structure in cathode, (d) line structure in anode, (e) cathode edge under an angle of 30°, (f) anode edge under an angle of 30°.

EDX of the electrodes was performed to analyze the surface composition and possible changes in the cathode composition in the laser-affected areas. The results of the analyses are shown in Figure 2a,b for the anode and cathode, respectively. At the surface of the anode, only carbon can be detected. It is assumed that there is only a very small amount of binder directly located on the surface, which would contain oxygen and hydrogen in addition to carbon, with the latter not being detectable through EDX analysis. The EDX analysis of the cathode's surface (Figure 2b) confirms that the cathode contains NMC 622 as an active material (17.7 at.% Ni, 6.6 at.% Mn, 6.3 at.% Co, 47.3 at.% O). The electrode also contains 22.1 at.% carbon, which is assumed to stem from the conductive agent or binder present in agglomerates. The EDX analysis of the laser-affected area reveals small amounts of aluminum, which originates from the current collector. The aluminum is uniformly distributed on the surface of the cathode, indicating that it was precipitated from the plasma or material vapor during laser ablation.

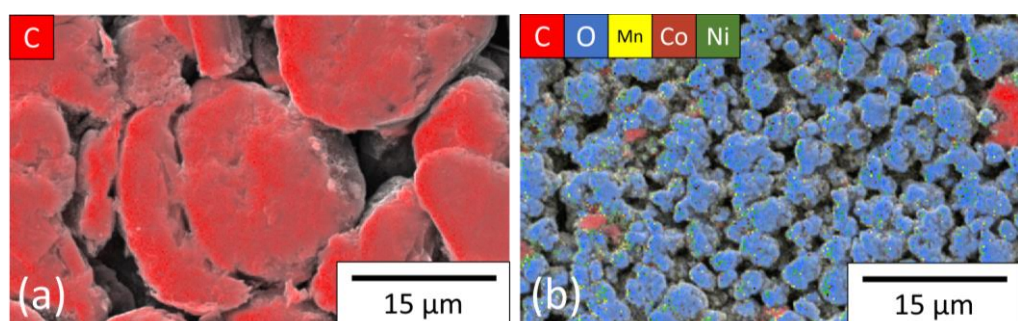


Figure 2. Results of the energy-dispersive X-ray spectroscopy surface mapping of the (a) anode and (b) cathode.

Very similar experimental conditions were applied in the publication by Dunlap et al. [22]. They also used graphite and NMC622 electrodes, the same laser wavelength and pulse length, and a similar beam diameter on the electrode surface. They applied FIB-SEM cross-sectional imaging, XRD, and EDX and found that very little damage was inflicted on the laser-impacted zones. For powder XRD, they found that no new peaks developed for the cathodes after laser patterning, which indicates that no new crystalline phases formed. But there was an increased degree of crystallinity and grain size near the channels. Despite high-temperature exposure during laser patterning, only negligible lithium loss and cation disordering were observed. The Rietveld fits before and after patterning showed a highly ordered structure. For the anode, the graphite lattice constants were calculated from Rietveld refinements of the XRD spectra and showed no change regardless of laser patterning. The graphite crystal domain size grew after laser patterning, indicating an annealing/aggregating effect of the laser patterning on the graphite. On the NMC cathode, cracks might occur, and some particles will be partially ablated. They concluded that due to the small amount of cracked or partially ablated particles compared to the total amount of particles, only an insignificant reduction in the electrochemical performance is expected, and no reduction was observed in the measurements. Kim et al. [23] also found that no peak shift was observed for the Raman spectrum of graphite electrodes after laser patterning.

We therefore conclude that even if small changes in the microstructure or chemistry occur, they will not be significant enough to change the electrochemical performance of the electrodes, and further investigations regarding the crystallography, chemistry, and morphology of the electrodes are outside of the scope of this manuscript.

Multilayer pouch cells with either structured or unstructured electrodes were assembled in pouch cells as described in the experimental section, and the electrochemical analysis was performed starting with the formation steps. At the formation step, capacities between 19.7 Ah and 21.1 Ah were achieved for cells with unstructured electrodes, while 14.7 Ah and 16.1 Ah were achieved for cells with structured electrodes.

The results of the differential capacity analysis for the first charge cycle during formation between 2.0 V and 3.4 V are shown in Figure 3. In this region of the dQ/dV diagram, the reduction potentials of EC and FEC (as electrolyte additive) are visualized. The reduction products form the passivation layer, the so-called solid electrolyte interface (SEI) [24], on the graphite particles of the anode. Between approx. 2.60 V and 2.88 V, the FEC is reduced [24,25]. When using structured electrodes, the FEC reduction starts at about 2.77 V, while it takes place at about 2.70 V for cells with unstructured electrodes. A small EC reduction peak at approximately 2.90 V [26,27] is found only for the cells with unstructured electrodes.

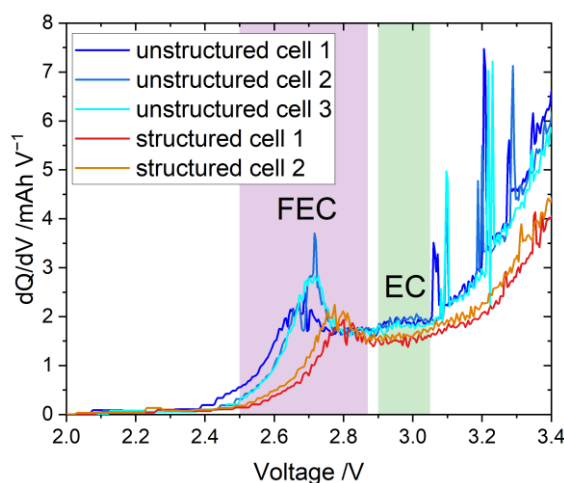


Figure 3. Results of the differential capacity analysis for the first charging during formation plotted versus the voltage, showing the formation of the solid electrolyte interface on the unstructured and laser-structured anodes. The regions of reduction potential of FEC and EC are highlighted in purple and green, respectively.

For cells with structured electrodes, the EC reduction peak is greatly reduced in intensity. At approx. 3.05 V to 3.09 V, 3.19 V to 3.23 V, and 3.28 V, additional peaks can be identified for the cells with unstructured electrodes, indicating further reduction processes, while for those containing laser-structured electrodes, these peaks do not appear. These additional peaks have not been described in the literature and further studies are required to properly attribute them. So far, it is assumed that the observed difference in the dQ/dV analysis might be caused by the fact that the structured electrodes provide electrolyte reservoirs that are activated already during the electrochemical formation, which in turn could affect the time sequence in the formation of the SEI passivation layers. In addition, possible deficiencies in the electrolyte (and electrolyte additives) can be counteracted and a more stable SEI could be formed when using structured electrodes.

The results of the first (dashed line) and second (solid line) cycle dQ/dV analysis of the formation steps are shown in Figure 4. A Savitzky–Golay smoothing filter (second polynomial order, window width 20) was applied to the raw data to facilitate peak identification. Three peaks can be identified for the charging step, i.e., c1, c2, and c3, and two peaks and a plateau can be identified for the discharging step, i.e., d1, d2, and d3. The positions of the peaks and their corresponding phase transitions are summarized in Table 1. The peaks at c1 and c2 can be associated with the lithiation of graphite and the phase transition from a hexagonal (H1) to monoclinic (M) lattice in the layered oxide [28–30]. The peak at c3 is associated with a phase transition from monoclinic to rhombohedral (H2) [28–31]. During delithiation, the processes take place in reverse order, i.e., d3 can be linked to the phase transition from rhombohedral to monoclinic, and c2 and c1 can be associated with the delithiation of graphite and the phase transition from monoclinic to hexagonal. Between c1 and c2, the monoclinic single-phase capacity is located and two additional peaks can be found that are also present in LiNiO₂ [32] or, to a lesser extent, in NMC 622 [33]. c3 shows

the largest difference between the cells with structured and unstructured electrodes. This has been associated with the changed n/p ratio of the unstructured (1.1) and structured (1.24) electrodes in [22].

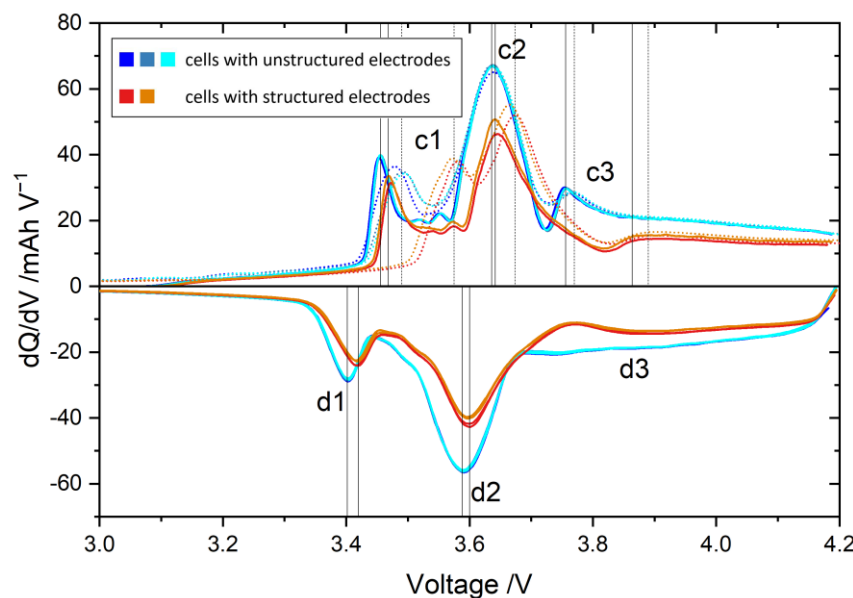


Figure 4. Differential capacity of the cells plotted against the voltage for all cells at the first (dashed line) and second (solid line) formation step; lines in shades of blue were used for cells with unstructured electrodes, lines in red and orange for cells with structured electrodes.

Table 1. Position of the peaks in the differential capacity analysis of the formation step and their corresponding phase transitions.

Unstructured		Structured		Phase Transition
1st Cycle	2nd Cycle	1st Cycle	2nd Cycle	
c1	3.49	3.46	3.58	3.47
c2	3.64	3.64	3.67	3.64
c3	3.77	3.76	3.89	3.86
d1	3.40	3.40	3.42	3.42
d2	3.59	3.59	3.60	3.60
d3	plateau between approx. 3.8 V and 4.2 V			H2 → M

A peak offset between charge and discharge can be observed for both cell types, which can be related to the effect of the cell impedance [34]. Considering the peak positions, a lower cell impedance can be associated with the cells with structured electrodes (peak offset between c1 and d1 is 0.05 V for structured cells and 0.06 V for unstructured ones; peak offset between c2 and d2 is 0.04 V for structured cells and 0.05 V for unstructured ones). Comparing the peak positions of the individual phase transitions, a shift to higher voltage values can be observed for cells with structured electrodes. In [22], a peak shift was also observed, but the peak position shifted from higher values to lower values, which was associated with a decrease in the cell overpotential. It is hypothesized that due to the excess electrolyte in the electrolyte reservoirs, generated by the laser patterning process, the formation of the SEI proceeds differently compared to cells with unstructured electrodes. This will also affect the curvature of the differential capacity analysis and the peak positions. Due to the higher amount of additives per weight of active material, a more stable SEI should be formed. It may be of interest to investigate the amount of FEC still detectable after the formation cycles depending on the laser patterning status of the electrodes.

After the formation, symmetric rate capability measurements were conducted between C-rates of C/10 and 5C, with the charge process using a CCCV protocol and the discharge process using a CC protocol. The results of the rate capability measurements (C/10 to 5C) are shown in Figure 5. The initial capacities at C/10 are 18.9 Ah to 20.0 Ah for the cells with unstructured electrodes, and 14.5 Ah to 15.0 Ah for the cells with structured electrodes (see Figure 5a). The lower capacity is due to the ablated active materials in laser-structured electrodes, which is consistent with the mass loss in the NMC 622 cathode. As the C-rate increases, the capacity decreases for all cells.

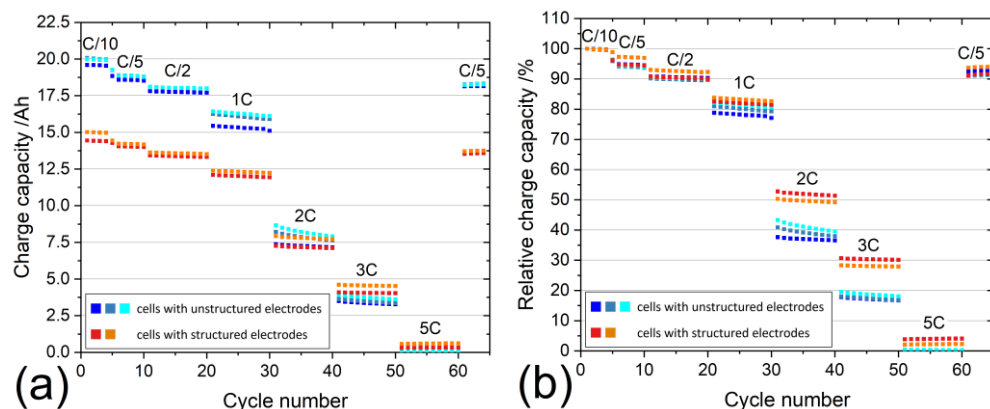


Figure 5. Rate capability measurements of the pouch cells: (a) charge capacity and (b) relative charge capacity.

At 2C, the cells with structured electrodes reach similar capacities compared to the cells with unstructured electrodes, while at 3C, the capacities of the cells with structured electrodes exceed the capacities of the reference cells with the unstructured electrodes. After cycling at 5C, the cells were cycled again at C/5, and the capacity retentions are 98.1%, 97.3%, and 97.2% for the cells with unstructured electrodes and 96.3% and 96.8% for the cells with structured electrodes, indicating that no severe degradation has occurred. The relative charge capacities are shown in Figure 5b. Higher relative capacities can be measured for cells with structured electrodes at a C-rate of 1C. At C-rates of 2C and 3C, a 10% increase in relative capacity can be achieved compared to the reference cells. This can be related to a reduced tortuosity, ohmic polarization, and overpotential of the cells with structured electrodes, as it has been described in [12,15,17,18,20].

The normalized discharge voltage profiles for a representative cell with unstructured electrodes and a cell with structured electrodes for three exemplary C-rates (C/10, 1C, and 3C) are shown in Figure 6. They have been normalized to a capacity scale of 0–1 to ensure better comparability even though different total capacities were achieved. With increasing C-rate, the IR drop and the ohmic polarization increase. This was also found, for example, in [35] for NMC 622 and other NMC-type active materials. For the cells with unstructured electrodes, the IR drop and the ohmic polarization are increased more compared to cells with structured electrodes.

Figure 7a displays the average charge capacity of cells containing either unstructured or structured electrodes derived from the CC and CV phases of the charge rate test. At C/10 and C/5, cells with unstructured electrodes show about a 5.3 Ah higher total capacity than those with structured electrodes. This corresponds to the 22.3% mass loss on the NMC 622 cathode side due to the laser structuring. The total charge capacity decreases with increasing C-rate. For example, the total capacity of cells with unstructured electrodes decreases from 20 Ah to 4 Ah as the C-rate increases from C/10 to 3C, retaining 20% of capacity in comparison to the initial capacity, while those with structured electrodes exhibit a smaller capacity decrease from 15 Ah to 10 Ah under the same conditions, with 31% of the capacity remaining. When the C-rate is higher than 2C, it is found that most of the charge capacity comes from the CV phase. The proportions of charge capacity originating from the

CC and CV phase as well as the relative total capacity versus the initial capacity at C/10 are presented in Figure 7b. With increasing C-rate from C/10 to 2C, the CV-phase capacity fraction of cells with unstructured electrodes increases from 1.5% to 89.4%, while that of cells with laser-structured electrodes increases from 1.3% to 74.3%. At 3C, the CC-phase capacity fraction of cells with laser-structured electrodes still takes up 1.2%, while cells with unstructured electrodes exhibit a 0% CC capacity share at 3C and 5C, indicating that the cells have been charged only through the CV phase.

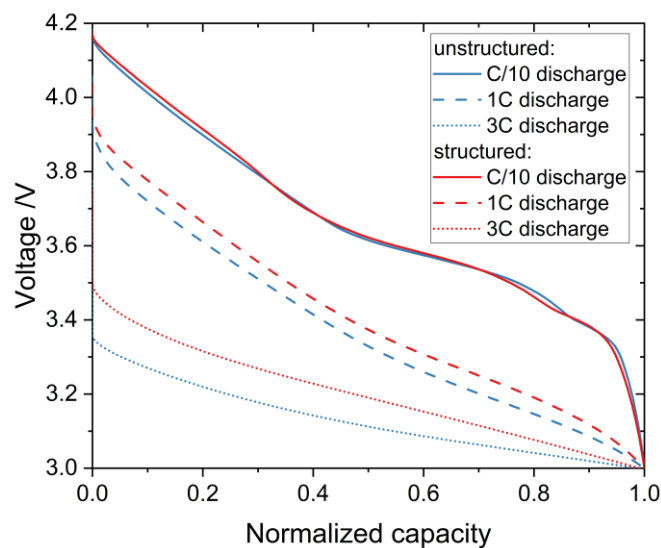


Figure 6. Constant-current discharge voltage profiles of selected cells and cycles during a C/10 to 5C rate capability test.

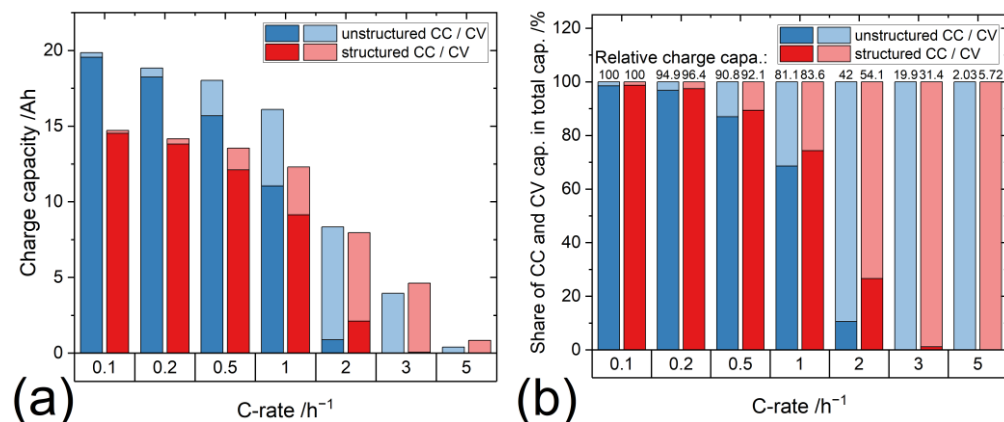


Figure 7. Charge capacity of the cells: (a) total capacity and (b) share of CC and CV capacity in total charge capacity for unstructured and structured electrodes.

In order to investigate the effect of laser structuring on the practical charging and discharging times of cells at different C-rates, the mean charging time, the proportion of charging times derived from CC and CV phases, as well as ratio of discharging time to charging time are shown in Figure 8a–c. In Figure 8a, cells with unstructured electrodes reach a total charge time of 9.9 h at C/10, while those with laser-structured electrodes show a total charge time of 9.2 h, indicating that a higher specific current was applied for the charging process in cells with laser-structured electrodes. Considering the mass loss of 22.3% of the cathode, the specific current for the structured electrodes was 17.05 mA g^{-1} , while the current for the unstructured electrodes was 16.63 mA g^{-1} at a C-rate of C/10. As the C-rate increases to C/5, the difference in charging time between cells with unstructured and laser-structured electrodes is reduced, i.e., the ones with unstructured electrodes

exhibit 4.7 h of charging time, while the cells with laser-structured electrodes reach 4.4 h of charging time. At C/2 to 2C, cells with unstructured electrodes show a 0.1 h longer charging time in contrast to those with laser-structured electrodes, while at 3C and 5C, an opposite trend is observed, where cells with laser-structured electrodes exhibit 0.1 h more charging time in comparison to those with unstructured electrodes. However, the cells should be theoretically charged in 0.5 h at 2C, but both cells with unstructured and laser-structured electrodes show a charging time of about 0.7 h, which comes from the CV phase. Similarly, all cells exhibit a 0.5 h charging time at 3C, which is significantly higher in comparison to 0.33 h and only stems from the CV phase. The shares of charging time from the CC and CV phase in contrast to the total charging time are displayed in Figure 8b. By comparing this figure with Figure 7b, a similar trend is observed: (i) the proportion of charging time/capacity from the CC phase decreases with increasing C-rates, and (ii) the cells with laser-structured electrodes maintain a higher share of charging time/capacity at higher C-rates $\geq C/2$. Figure 8c compares the ratio of discharge to charging time of cells at different C-rates. The ratios of all cells decrease with increasing C-rates, while the cells with unstructured electrodes display lower ratios compared to those with laser-structured electrodes at each C-rate. The low ratios of cells with unstructured electrodes indicate that the discharging time of cells with unstructured electrodes is shorter in contrast to those with laser-structured electrodes, which is consistent with the lower charge capacity of cells with unstructured electrodes, especially at C-rates higher than 1C.

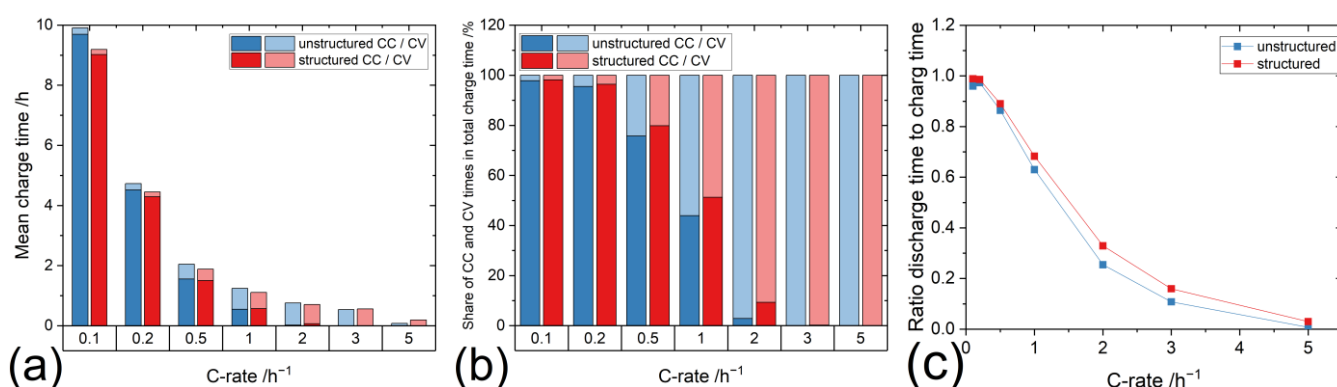


Figure 8. (a) Mean charge times; (b) share of CC and CV charge times on total charge time; and (c) ratio of discharge times to charge times for the cells with unstructured and structured electrodes.

Lifetime analysis (cycling at 1C) of the pouch cells is shown in Figure 9a–c. For a detailed analysis of the charging behavior, the charge capacities are divided into the capacity derived from the CC and CV phases. Figure 9 shows that the cells with unstructured electrodes have an initial total charge capacity of 14.1 Ah to 14.4 Ah, while the cells with structured electrodes show a capacity of 11.7 Ah and 11.9 Ah. All cells exhibit a decreasing total charge or discharge capacity with increasing cycle number, while the gradient of the capacity drop is higher for the cells with unstructured electrodes, indicating a lower cell polarization in the cells with structured electrodes in comparison to the reference cells. The CC charge capacity decreases with increasing cycle number, while the CV capacity increases. It is worth noting that the charge capacity increase in the CV phase for the cells with unstructured electrodes is 9.6% to 13% compared to 2.7% and 4.2% for those with structured electrodes after 100 cycles, which indicates that more capacity stems from the CC phase instead of the CV phase during the aging test for cells with laser-structured electrodes. This can be associated with the lower internal cell resistance due to the increased electrode surface, which was also shown in [8,19]. After ~ 140 full cycles, the cells with structured electrodes show higher charge and discharge capacities than the reference cells do. For the cells with unstructured electrodes, the End-of-Life (EoL) at 80% of relative capacity is reached after 96, 117, and 123 cycles. However, cells with structured electrodes

maintain 89% of capacity after 350 cycles, which indicates that the aging process of cells with laser-patterned electrodes is mitigated.

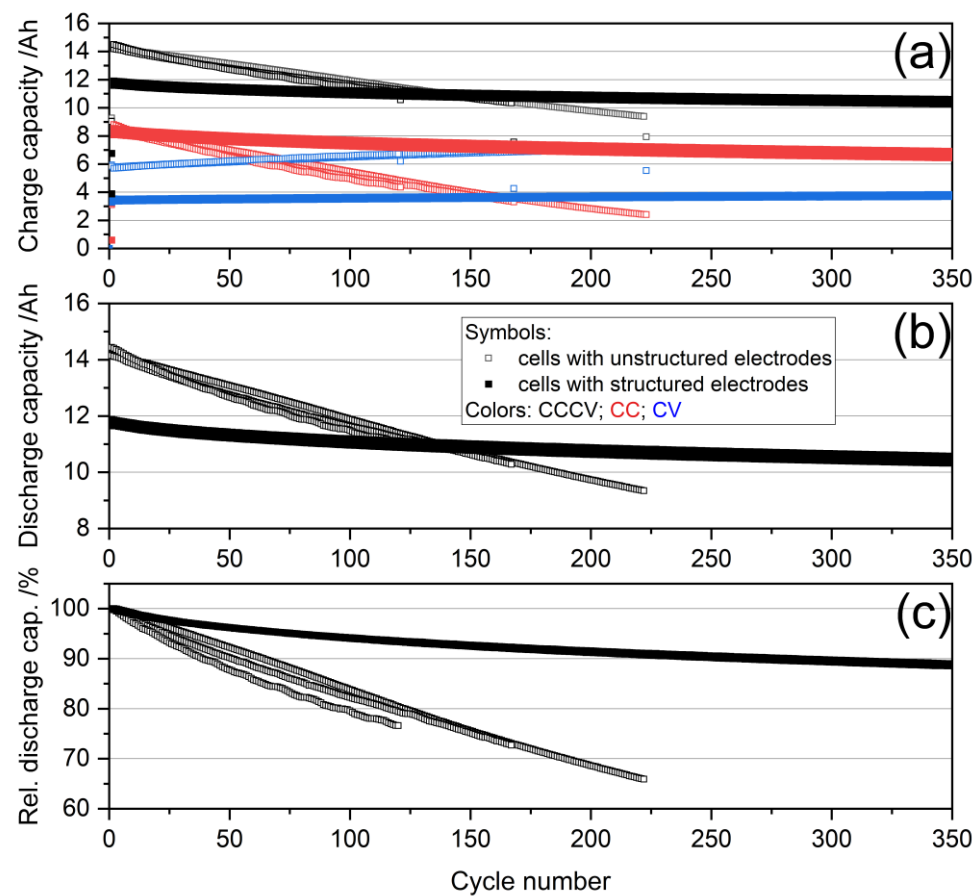


Figure 9. Lifetime analyses of the pouch cells. Open symbols: unstructured electrodes; solid symbols: structured electrodes. (a) Charge capacities: black, CCCV; red, CC; blue, CV. (b) Discharge capacities. (c) Relative discharge capacities.

In the study by Kriegler et al. [11], NMC 111 cathodes with an areal loading of 1.98 mAh/cm² were used, while exclusively laser-patterned graphite anodes were applied. The cells with an initial capacity of 2.9 Ah exhibited 77% of relative capacity after 300 cycles at 4C charging (CCCV with a cut-off current of C/20) and C/2 discharging. The 4C CC charging resulted in a capacity of 1.36 Ah, with 0.88 Ah charged during CV charging. In the study by Dunlap et al. [22], NMC 622 cathodes and graphite anodes were laser structured with a line pattern. The NMC 622 cathodes showed theoretical areal loadings of 4.28 mAh/cm² (pristine) and 3.81 mAh/cm² (structured), while the anodes had loadings of 4.35 mAh/cm² (pristine) and 3.61 mAh/cm² (laser patterned). The electrodes were assembled in coin cells, and a capacity retention of 52.9% was obtained after cycling for 100 cycles at 6C (6C CC charging until reaching 4.2 V, then CV charging until a total charge time of 10 min). The findings of this research demonstrate a noteworthy enhancement compared to the previous studies. The lithium-ion diffusion pathway from the liquid electrolyte to the active particles at the bottom of bulk electrodes near the current collector is shortened due to the laser patterning, as the lithium-ion insertion from the sidewalls of the channel structures is facilitated, reducing the tortuosity of the electrode, as verified in [6,7] through laser-induced breakdown spectroscopy. In contrast, the reference electrodes require lithium ions to diffuse through the compacted composite material. The concentration of lithium in cycled electrodes with laser-generated patterns is quite uniform compared to lithium distributions in unstructured electrodes. The latter normally show a considerable concentration gradient from the top of the electrode to the current collector [6,7]. As a

result, in the case of applying a 3D electrode architecture, the electrochemical reaction can involve significantly more active material particles near the current collector.

The normalized charge–discharge curves for cells with unstructured and structured electrodes for selected cycles during long-term testing are shown in Figure 10. The cell capacities are continually decreasing due to an increasing cell polarization. The average discharge voltage is lowered, which decreases the deliverable capacity, since the cut-off voltage is kept constant at 3.0 V. The IR drop and ohmic polarization demonstrate an increase as the cycles progress, as indicated by the arrows in Figure 10. Upon the comparison of cells with unstructured and structured electrodes, it becomes apparent that the IR drop and the ohmic polarization increase more for cells with unstructured electrodes. These results may imply continuous SEI growth [36]. Similar observations were made in the past, such as in [37].

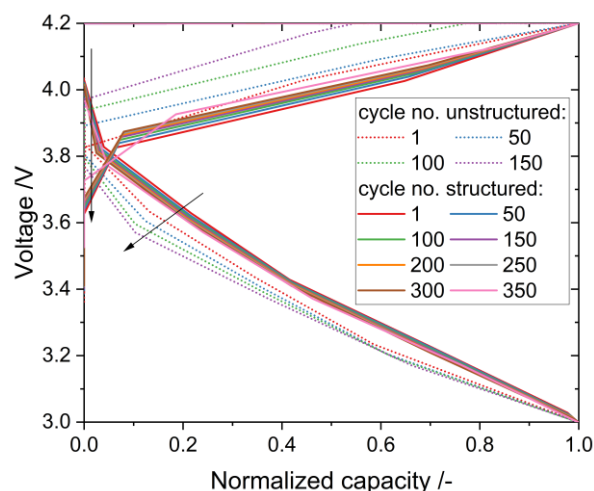


Figure 10. Normalized charge and discharge voltage profiles of the cells during long-term testing at 1C for structured (solid line) and unstructured (dashed line) electrodes in comparison. Arrows indicate trends of IR drop and ohmic resistance.

4. Conclusions

Commercially available NMC 622 cathodes (4.0 mAh cm^{-2}) and graphite anodes (4.4 mAh cm^{-2}) were patterned using a high-power USP laser with a pulse length of 600 fs and a repetition rate of 1 MHz. The laser patterning was executed in a roll-to-roll environment, validating its feasibility for process scaling (technology readiness level TRL 6). Scanning electron microscopy images confirmed the attainment of line structures down to the current collector without any crack formation or debris. The aspect ratio was approximately 1.5 for both electrode types. Energy-dispersive X-ray spectroscopy measurements indicated no chemical alteration or melting of the active materials near the channel structures. Pouch cells containing a multi-electrode stack were assembled with nine cathodes and ten anodes, using either unstructured or structured electrodes to yield mean total capacities of approximately 20.4 Ah and 15.4 Ah, respectively. The peaks of the formations in differential capacity analysis indicated a shift due to the laser structuring, which could be attributed to the electrolyte reservoirs and the greater electrolyte-to-active-material ratio in laser-patterned electrodes. In addition, cells containing laser-patterned electrodes demonstrated an enhanced performance in rate capability analyses between 1C and 5C, with a reduced ohmic polarization and IR drop. In addition, the proportion of the CC charging in the overall charged capacity is greater with the structured electrodes. Symmetrical lifetime tests at 1C by applying 100% of DoD (depth of discharge) confirmed a vastly improved longevity of the cells with patterned electrodes, showing 89% of discharge capacity after 350 cycles, while cells with reference electrodes showed an EoL (80% of retained capacity) after 110 full cycles.

Author Contributions: Conceptualization, W.P., A.M. and P.Z.; methodology, W.P., A.M. and P.Z.; validation, A.S. and A.M.; investigation, A.M., P.Z. and A.S.; resources, W.P. and A.S.; data curation, A.M.; writing—original draft preparation, A.M.; writing—review and editing, W.P., P.Z. and A.S.; visualization, A.M.; supervision, W.P.; project administration, W.P.; funding acquisition, W.P. All authors have read and agreed to the published version of the manuscript.

Funding: This research was funded by the German Federal Ministry of Education and Research (BMBF), project NextGen-3DBat, grant number 03XP0198F.

Data Availability Statement: Data are contained within the article.

Acknowledgments: We would like to thank Olivia Wiegand and Steffen Jokisch for the assembly and the cycling of the cells, respectively, which was performed at KIT-BATEC. This work contributes to the research performed at the Center for Electrochemical Energy Storage Ulm & Karlsruhe (CELEST).

Conflicts of Interest: The authors declare no conflict of interest.

References

1. Long, J.W.; Dunn, B.; Rolison, D.R.; White, H.S. Three-dimensional battery architectures. *Chem. Rev.* **2004**, *104*, 4463–4492. [[CrossRef](#)] [[PubMed](#)]
2. Pfleger, W.; Pröll, J. A new approach for rapid electrolyte wetting in tape cast electrodes for lithium-ion batteries. *J. Mater. Chem. A* **2014**, *2*, 14918–14926. [[CrossRef](#)]
3. Pfleger, W. A review of laser electrode processing for development and manufacturing of lithium-ion batteries. *Nanophotonics* **2018**, *7*, 549–573. [[CrossRef](#)]
4. Pfleger, W. Recent progress in laser texturing of battery materials: A review of tuning electrochemical performances, related material development, and prospects for large-scale manufacturing. *Int. J. Extrem. Manuf.* **2021**, *3*, 12002. [[CrossRef](#)]
5. Habedank, J.B.; Günter, F.J.; Billot, N.; Gilles, R.; Neuwirth, T.; Reinhart, G.; Zaeh, M.F. Rapid electrolyte wetting of lithium-ion batteries containing laser structured electrodes: In situ visualization by neutron radiography. *Int. J. Adv. Manuf. Technol.* **2019**, *102*, 2769–2778. [[CrossRef](#)]
6. Smyrek, P.; Bergfeldt, T.; Seifert, H.J.; Pfleger, W. Laser-induced breakdown spectroscopy for the quantitative measurement of lithium concentration profiles in structured and unstructured electrodes. *J. Mater. Chem. A* **2019**, *7*, 5656–5665. [[CrossRef](#)]
7. Zheng, Y.; Pfäffl, L.; Seifert, H.J.; Pfleger, W. Lithium Distribution in Structured Graphite Anodes Investigated by Laser-Induced Breakdown Spectroscopy. *Appl. Sci.* **2019**, *9*, 4218. [[CrossRef](#)]
8. Park, J.; Song, H.; Jang, I.; Lee, J.; Um, J.; Bae, S.; Kim, J.; Jeong, S.; Kim, H.-J. Three-dimensionilization via control of laser-structuring parameters for high energy and high power lithium-ion battery under various operating conditions. *J. Energy Chem.* **2022**, *64*, 93–102. [[CrossRef](#)]
9. Pröll, J.; Kohler, R.; Mangang, A.; Ulrich, S.; Ziebert, C.; Pfleger, W. 3D Structures in Battery Materials. *J. Laser Micro/Nanoeng.* **2012**, *7*, 97–104. [[CrossRef](#)]
10. Kohler, R.; Smyrek, P.; Ulrich, S.; Bruns, M.; Trouillet, V.; Pfleger, W. Patterning and annealing of nanocrystalline LiCoO₂ thin films. *J. Optoelectron. Adv. Mater.* **2010**, *12*, 547–552.
11. Kriegler, J.; Hille, L.; Stock, S.; Kraft, L.; Hagemeister, J.; Habedank, J.B.; Jossen, A.; Zaeh, M.F. Enhanced performance and lifetime of lithium-ion batteries by laser structuring of graphite anodes. *Appl. Energy* **2021**, *303*, 117693. [[CrossRef](#)]
12. Habedank, J.B.; Endres, J.; Schmitz, P.; Zaeh, M.F.; Huber, H.P. Femtosecond laser structuring of graphite anodes for improved lithium-ion batteries: Ablation characteristics and process design. *J. Laser Appl.* **2018**, *30*, 32205. [[CrossRef](#)]
13. Chen, K.-H.; Namkoong, M.J.; Goel, V.; Yang, C.; Kazemiannavi, S.; Mortuza, S.M.; Kazyak, E.; Mazumder, J.; Thornton, K.; Sakamoto, J.; et al. Efficient fast-charging of lithium-ion batteries enabled by laser-patterned three-dimensional graphite anode architectures. *J. Power Sources* **2020**, *471*, 228475. [[CrossRef](#)]
14. Yamada, M.; Soma, N.; Tsuta, M.; Nakamura, S.; Ando, N.; Matsumoto, F. Development of a roll-to-roll high-speed laser micro processing machine for preparing through-holed anodes and cathodes of lithium-ion batteries. *Int. J. Extrem. Manuf.* **2023**, *5*, 35004. [[CrossRef](#)]
15. Meyer, A.; Ball, F.; Pfleger, W. The Effect of Silicon Grade and Electrode Architecture on the Performance of Advanced Anodes for Next Generation Lithium-Ion Cells. *Nanomaterials* **2021**, *11*, 3448. [[CrossRef](#)]
16. Zheng, Y.; Seifert, H.J.; Shi, H.; Zhang, Y.; Kübel, C.; Pfleger, W. 3D silicon/graphite composite electrodes for high-energy lithium-ion batteries. *Electrochim. Acta* **2019**, *317*, 502–508. [[CrossRef](#)]
17. Zheng, Y.; Smyrek, P.; Rakebrandt, J.-H.; Kübel, C.; Seifert, H.J.; Pfleger, W. Fabrication and characterization of silicon-based 3D electrodes for high-energy lithium-ion batteries. *Proc. SPIE* **2017**, *10092*, 100920L-1–100920L-8.
18. Zhu, P.; Seifert, H.J.; Pfleger, W. The Ultrafast Laser Ablation of Li(Ni_{0.6}Mn_{0.2}Co_{0.2})O₂ Electrodes with High Mass Loading. *Appl. Sci.* **2019**, *9*, 4067. [[CrossRef](#)]
19. Pfleger, W.; Gotcu, P. Femtosecond Laser Processing of Thick Film Cathodes and Its Impact on Lithium-Ion Diffusion Kinetics. *Appl. Sci.* **2019**, *9*, 3588. [[CrossRef](#)]

20. Zhu, P.; Han, J.; Pfleging, W. Characterization and Laser Structuring of Aqueous Processed $\text{Li}(\text{Ni}_{0.6}\text{Mn}_{0.2}\text{Co}_{0.2})\text{O}_2$ Thick-Film Cathodes for Lithium-Ion Batteries. *Nanomaterials* **2021**, *11*, 1840. [[CrossRef](#)]
21. Smith, A.; Stüble, P.; Leuthner, L.; Hofmann, A.; Jeschull, F.; Mereacre, L. Potential and Limitations of Research Battery Cell Types for Electrochemical Data Acquisition. *Batter. Supercaps* **2023**, *6*, e202300080. [[CrossRef](#)]
22. Dunlap, N.; Sulas-Kern, D.B.; Weddle, P.J.; Usseglio-Viretta, F.; Walker, P.; Todd, P.; Boone, D.; Colclasure, A.M.; Smith, K.; Tremolet de Villers, B.J.; et al. Laser ablation for structuring Li-ion electrodes for fast charging and its impact on material properties, rate capability, Li plating, and wetting. *J. Power Sources* **2022**, *537*, 231464. [[CrossRef](#)]
23. Kim, Y.; Drews, A.; Chandrasekaran, R.; Miller, T.; Sakamoto, J. Improving Li-ion battery charge rate acceptance through highly ordered hierarchical electrode design. *Ionics* **2018**, *24*, 2935–2943. [[CrossRef](#)]
24. Logan, E.R.; Hebecker, H.; Ma, X.; Quinn, J.; HyeJeong, Y.; Kumakura, S.; Paulsen, J.; Dahn, J.R. A Comparison of the Performance of Different Morphologies of $\text{LiNi}_{0.8}\text{Mn}_{0.1}\text{Co}_{0.1}\text{O}_2$ Using Isothermal Microcalorimetry, Ultra-High Precision Coulometry, and Long-Term Cycling. *J. Electrochem. Soc.* **2020**, *167*, 60530. [[CrossRef](#)]
25. Yoo, D.-J.; Liu, Q.; Cohen, O.; Kim, M.; Persson, K.A.; Zhang, Z. Rational Design of Fluorinated Electrolytes for Low Temperature Lithium-Ion Batteries. *Adv. Energy Mater.* **2023**, *13*, e202204182. [[CrossRef](#)]
26. Gauthier, R.; Hall, D.S.; Lin, K.; Baltazar, J.; Hynes, T.; Dahn, J.R. Impact of Functionalization and Co-Additives on Dioxazolone Electrolyte Additives. *J. Electrochem. Soc.* **2020**, *167*, 80540. [[CrossRef](#)]
27. Hall, D.S.; Hynes, T.; Dahn, J.R. Dioxazolone and Nitrile Sulfite Electrolyte Additives for Lithium-Ion Cells. *J. Electrochem. Soc.* **2018**, *165*, A2961–A2967. [[CrossRef](#)]
28. Jung, R.; Metzger, M.; Maglia, F.; Stinner, C.; Gasteiger, H.A. Oxygen Release and Its Effect on the Cycling Stability of LiNixMnyCozO_2 (NMC) Cathode Materials for Li-Ion Batteries. *J. Electrochem. Soc.* **2017**, *164*, A1361–A1377. [[CrossRef](#)]
29. Landa-Medrano, I.; Eguia-Barrio, A.; Sananes-Israel, S.; Lijó-Pando, S.; Boyano, I.; Alcaide, F.; Urdampilleta, I.; de Meatza, I. In Situ Analysis of NMC|graphite Li-Ion Batteries by Means of Complementary Electrochemical Methods. *J. Electrochem. Soc.* **2020**, *167*, 90528. [[CrossRef](#)]
30. Liu, T.; Yu, L.; Liu, J.; Lu, J.; Bi, X.; Dai, A.; Li, M.; Li, M.; Hu, Z.; Ma, L.; et al. Understanding Co roles towards developing Co-free Ni-rich cathodes for rechargeable batteries. *Nat. Energy* **2021**, *6*, 277–286. [[CrossRef](#)]
31. Biasi, L.d.; Schwarz, B.; Brezesinski, T.; Hartmann, P.; Janek, J.; Ehrenberg, H. Chemical, Structural, and Electronic Aspects of Formation and Degradation Behavior on Different Length Scales of Ni-Rich NCM and Li-Rich HE-NCM Cathode Materials in Li-Ion Batteries. *Adv. Mater.* **2019**, *31*, e1900985. [[CrossRef](#)] [[PubMed](#)]
32. Li, H.; Zhang, N.; Li, J.; Dahn, J.R. Updating the Structure and Electrochemistry of $\text{Li}_{x}\text{NiO}_2$ for $0 \leq x \leq 1$. *J. Electrochem. Soc.* **2018**, *165*, A2985–A2993. [[CrossRef](#)]
33. Liu, T.; Du, Z.; Wu, X.; Rahman, M.M.; Nordlund, D.; Zhao, K.; Schulz, M.D.; Lin, F.; Wood, D.L.; Belharouak, I. Bulk and surface structural changes in high nickel cathodes subjected to fast charging conditions. *Chem. Commun.* **2020**, *56*, 6973–6976. [[CrossRef](#)] [[PubMed](#)]
34. Gauthier, R.; Luscombe, A.; Bond, T.; Bauer, M.; Johnson, M.; Harlow, J.; Louli, A.; Dahn, J.R. How do Depth of Discharge, C-rate and Calendar Age Affect Capacity Retention, Impedance Growth, the Electrodes, and the Electrolyte in Li-Ion Cells? *J. Electrochem. Soc.* **2022**, *169*, 020518. [[CrossRef](#)]
35. Noh, H.-J.; Youn, S.; Yoon, C.S.; Sun, Y.-K. Comparison of the structural and electrochemical properties of layered $\text{Li}[\text{NixCoyMnz}]\text{O}_2$ ($x = 1/3, 0.5, 0.6, 0.7, 0.8$ and 0.85) cathode material for lithium-ion batteries. *J. Power Sources* **2013**, *233*, 121–130. [[CrossRef](#)]
36. Niu, C.; Liu, D.; Lochala, J.A.; Anderson, C.S.; Cao, X.; Gross, M.E.; Xu, W.; Zhang, J.-G.; Whittingham, M.S.; Xiao, J.; et al. Balancing interfacial reactions to achieve long cycle life in high-energy lithium metal batteries. *Nat. Energy* **2021**, *6*, 723–732. [[CrossRef](#)]
37. Quilty, C.D.; Bock, D.C.; Yan, S.; Takeuchi, K.J.; Takeuchi, E.S.; Marschilok, A.C. Probing Sources of Capacity Fade in $\text{LiNi}_{0.6}\text{Mn}_{0.2}\text{Co}_{0.2}\text{O}_2$ (NMC622): An Operando XRD Study of Li/NMC622 Batteries during Extended Cycling. *J. Phys. Chem. C* **2020**, *124*, 8119–8128. [[CrossRef](#)]

Disclaimer/Publisher's Note: The statements, opinions and data contained in all publications are solely those of the individual author(s) and contributor(s) and not of MDPI and/or the editor(s). MDPI and/or the editor(s) disclaim responsibility for any injury to people or property resulting from any ideas, methods, instructions or products referred to in the content.